RESEARCH ARTICLE

**ADVANCED
PHOTONICS
RESEARCH**
Open Access

www.adpr-journal.com

Optically Selective Neuron Stimulation with a Wavefront Shaping-Empowered Multimode Fiber

Tianting Zhong, Zhihai Qiu, Yong Wu, Jinghui Guo, Huanhao Li, Zhipeng Yu, Shengfu Cheng, Yingying Zhou, Jiejun Zhu, Jie Tian,* Lei Sun,* and Puxiang Lai*

Optogenetics is proved to be a powerful tool for exploring the connection between behavior and neural circuits. The progress greatly benefits from the advances of optical techniques that enable high spatiotemporal resolution for selective single-neuron stimulation through modulating light. Efficient propagation of modulated light, however, is handicapped by strong optical scattering in biological tissues, which results in inherent tradeoff between penetration depth and resolution. Schemes like graded index (GRIN) lens-based microendoscopes are developed to yield more confined delivery of light, but tissue damage caused by the insertion of the bulky components cannot be ignored. Herein, an optically selective precise neuron stimulation using an ultrathin multimode fiber (MMF) is demonstrated, which is empowered by optical wavefront shaping to achieve light focusing and rapid raster scanning without mechanical movement at the distal end of the MMF and even through a mouse skull. With this method, primary neurons expressing Chr2 can be regulated spatiotemporally in experiment. Although a lot shall be further improved, the work may open up new venues for noninvasive or minimally invasive all-optical investigation of neural circuits in used-to-be optically inaccessible brain regions.

1. Introduction

Selective stimulation of neuron cells at high spatiotemporal resolution in deep brain is a major goal in neuroscience.[1–3] Research indicates that neurons can sense, transduce, and respond to various external stimuli such as electric, magnetic, heat, and mechanical stimuli.[4,5] Unmodified neurons may be stimulated directly to evoke action potentials with external fields,

such as deep brain stimulation (DBS),[4] but such techniques lacked specificity and selectivity to individual neurons. To address that, in the so-called "optogenetics," chosen neurons can be selectively inserted with well-characterized light sensitive proteins (e.g., opsins) and enabled to respond to light stimulation, while other cells remain silent.[6,7] It enables precise neural manipulation with specific time sequence.[4,5,8] Such advancement of spatial resolution and specificity has made optogenetics a powerful tool in neuroscience, especially in exploring the connection between behavior and neural circuits and in treating brain diseases.

However, it usually requires invasive procedures to deliver photons into deep brain regions as skull and brain tissue have strong scattering effects to visible and near-infrared light which is often used in optogenetics. Practically, one may insert a thin optical fiber into a specific deep brain region for neuron activation, which allows for free moving animal manipulations in vivo. The output light from the fiber, no matter it is single-mode fiber (SMF) or multimode fiber (MMF), is divergent and characterized by a large illumination spot or random speckled pattern at a short distance away from the distal fiber end, which fails to meet the spatial variant of the neurons in the field of view (FOV). Although some groups reported that multitargets from a large FOV could be controlled and monitored via a tapered optical fiber,[9] single-fiber-

T. Zhong, Z. Qiu, Y. Wu, J. Guo, H. Li, Z. Yu, S. Cheng, Y. Zhou, J. Zhu,
L. Sun, P. Lai
Department of Biomedical Engineering
Hong Kong Polytechnic University
Hong Kong SAR, Hung Hom, Hong Kong
E-mail: lei.sun@polyu.edu.hk; puxiang.lai@polyu.edu.hk

T. Zhong, Z. Qiu, H. Li, Z. Yu, S. Cheng, Y. Zhou, P. Lai
Shenzhen Research Institute
Hong Kong Polytechnic University
Shenzhen 518057, China

(iD) The ORCID identification number(s) for the author(s) of this article can be found under https://doi.org/10.1002/adpr.202100231.

J. Guo
Department of Physiology
Faculty of Medicine
Jinan University
Guangzhou 510632, China

J. Tian
Beijing Advanced Innovation Center for Big Data-Based Precision Medicine
School of Medical Science and Engineering
Beihang University
Beijing 100191, China
E-mail: tian@ieee.org

J. Tian
Key Laboratory of Molecular Imaging
Institute of Automation
Chinese Academy of Sciences
Beijing 100190, China

based photon delivery technologies are unable to perform selective photoactivation at an adequate spatiotemporal precision and also recall a behavior involved in the circuits as it biases the temporal sequence of the firing pattern of the specific functions.[5,7] In this regard, optimizing the spatiotemporal resolution of light delivery is imperative in optogenetics at depths.

To overcome these limitations, various strategies have been proposed. Two major independent factors affecting the precision of optogenetics are of concern to explore, that is, photosensitive ion channels and optical illumination. The former includes the development of some new photosensitive ion channels that response on red-shifted light to increase the penetration of optogenetics.[10] Meanwhile, converting near-infrared light into blue light via upconversion mechanisms also can be utilized to reduce the need for invasion.[11] To increase the spatiotemporal resolution of optogenetics, Boyden et al., engineered a new opsin that only is expressed on the soma of the neuron and shows better spatial resolution under two-photon excitation.[12] The other orientation is to improve the way of illumination, in which controlling the light distribution in space and time within or after tissue or tissue sample is more challenging (**Figure 1**a). Two-photon holography-based techniques have been utilized to improve the spatial selections of the excitations (Figure 1b). Some studies demonstrated that opsins possessed excellent two-photon cross session that can be excited effectively and hence could induce sufficient photocurrent in the micrometer focal volume.[12–16] Combined with photosensitive ion channels mentioned earlier,

it can activate single neurons in vivo by illuminating specific neurons, enabling us to mimic the natural neuronal code of a specific behavior or brain state. That said, certain critical drawbacks need to be overcome. For example, because of the optical objective and the complex free space optical system, the method sees implementations only for head fixed rodent, confining its applications to nonfree moving animals. Also, the working distance is significantly limited. As reported so far, the penetration depths of those noninvasive high-resolution optogenetics are limited to ≈1 mm.[17] Beyond that, scattering and optical aberrations dominate within the brain tissue and prohibit observations for subcortical structures and precise activation of neurons. These areas are, however, involved with important neuronal processes such as memory formation and gating of sensory and motor information, as well as neurological diseases.[17–19] To explore these brain areas, especially in larger animals, the required working distance may be up to several centimeters. To deal with the strong scattering effect of skull and other biological tissues, invasive procedures may be needed to create optical window for light propagation. Or, alternatively, optical wavefront shaping can be adopted,[20–34] which has been reported to generate a diffraction-limit focus through the skull,[35] or within the brain.[36] These methods, however, encounter similar limitations with the two-photon based approaches: the complex optical setup could not be separated from the animal, that is, it also requires the animal head to be fixed.
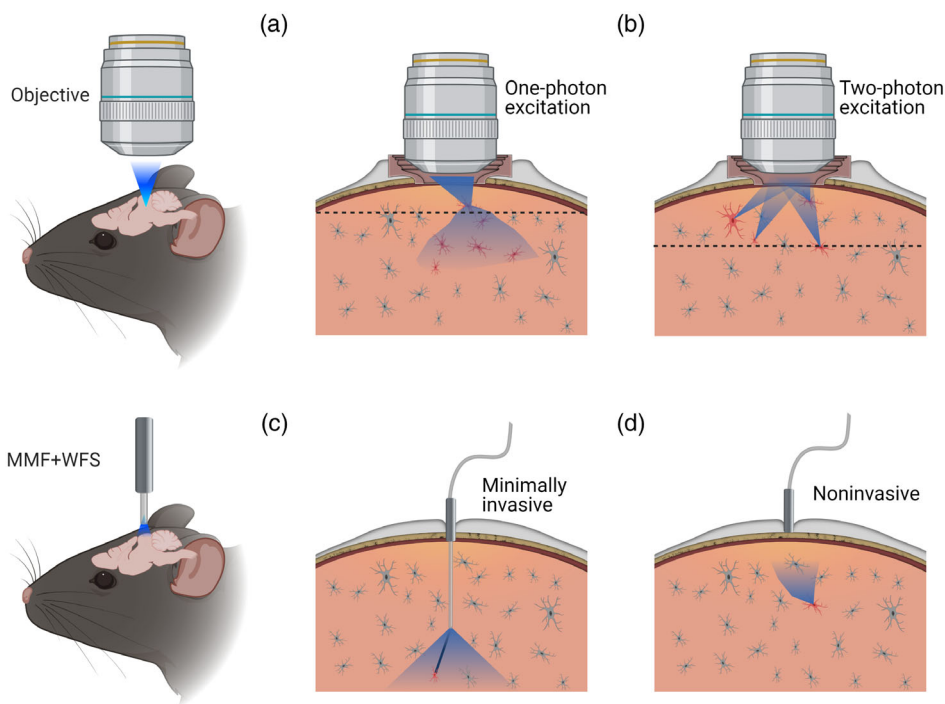

Figure 1. Schematics of current optical delivery methods for in vivo optogenetics and the proposed selective precise neuron stimulation concept. a) Diffused light caused by multiple light scattering in the brain tissues results in poor-resolution stimulation of neurons. b) Two-photon excitation with holographic modulation could stimulate single-target neurons and improve the working depths (indicated by dotted lines). c) The scattering of skull and brain tissues can be conquered via the insertion of MMF, which is minimally invasive and able to perform precise stimulation within a relatively large FOV by wavefront shaping. d) Focused light delivery can also be achieved through skull, enabling wearable noninvasive selective excitation of neurons at depths, which is otherwise impossible without the integration of wavefront shaping and MMF.

2100231 (2 of 11)

Unlike the previous strategies, nowadays, optical manipulation for selective single-neuron optogenetics in deep (more than ≈1 mm) brain areas is usually achieved by the combination of patterned light illumination approaches with endoscopic probes, such as graded index (GRIN) lenses[37–39] and fiber bundles.[40] While promising, these approaches create substantial mechanical lesions in tissue due to their large size, precipitating neuropathological responses that include inflammation and gliosis[41] and possibly ultimately compromising the physiology of neuronal networks and behavior of the animal.[42,43] Compared with these endoscopic probes, a single MMF could be much smaller to minimize the lesion problem. In this work, we propose an endoscopic approach that combines an MMF of compact size with wavefront shaping to achieve selective single-neuron optogenetics at depths (Figure 1c). The MMF can be regarded as a scattering medium and the output optical field from the MMF, originally being random speckled patterns, can be modulated to desired patterns.[44–53] In the proposed system, a digital micromirror device

(DMD) is utilized to manipulate the light propagation through the MMF. With wavefront shaping, the output field of MMF can be fully controlled (like generating static optical focus and hence raster scanning of the focus) once its transmission matrix (TM) is obtained. Such capacity of generating and scanning optical focus by wavefront shaping and its application for selective optogenetics is tested with cultured neurons. Moreover, the system can also enable sharp light focusing through the MMF and a mouse skull, demonstrating its competence for noninvasive selective activation of deep neurons through the skull with a high spatiotemporal resolution (Figure 1d).

2. Results

The fidelity of the generated foci determines the accuracy of the neuron stimulation. Without wavefront shaping, optical energy transmitting through the MMF spreads out at the output of the MMF, forming a seeming random speckled pattern (**Figure 2a**).
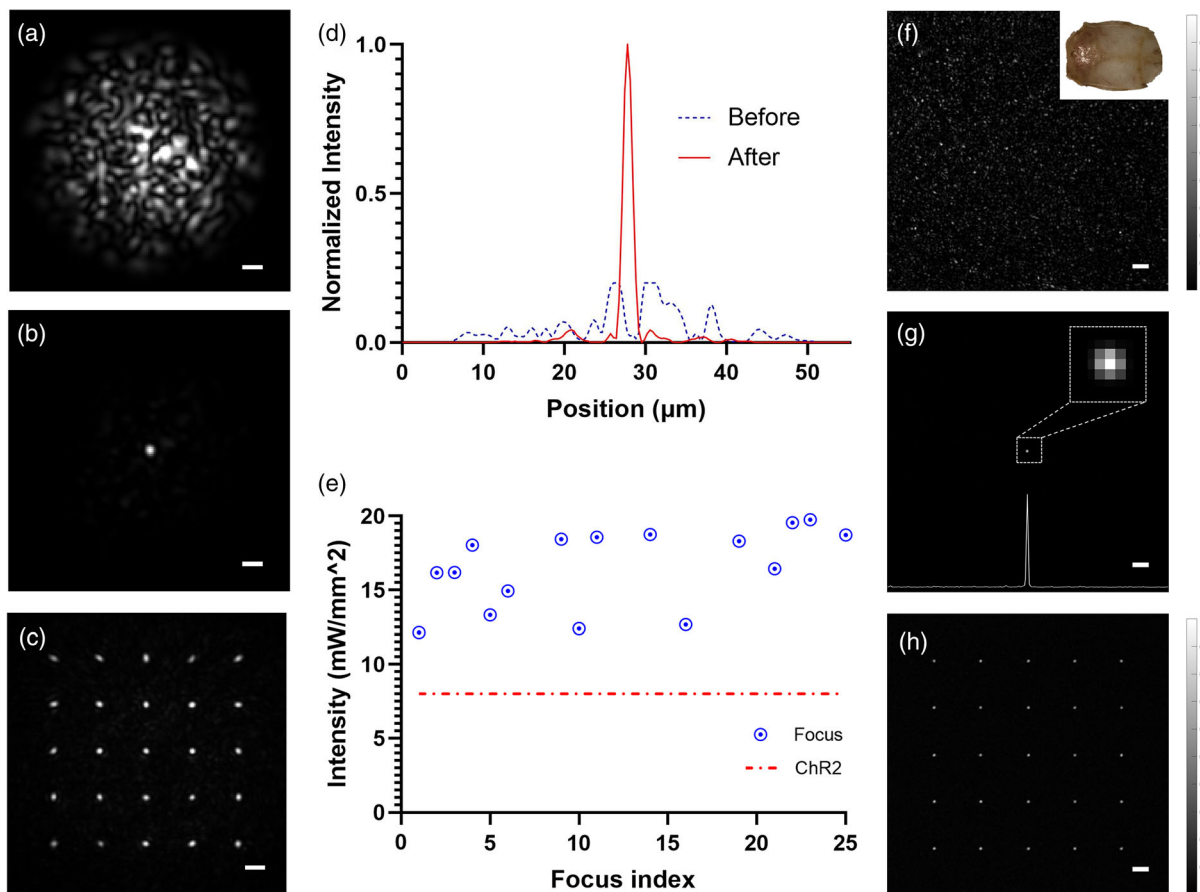

Figure 2. a,b) Images of the transmitted optical pattern through the MMF a) before and b) after (b) wavefront shaping. c) A series of foci can be formed one after another at the focal plane of the MMF FOV by "raster scanning" the phase patterns loaded on the DMD. d) Intensity profiles across the central focal position before and after wavefront shaping. e) Distribution of the focal intensities of the sample 25 focuses through raster scanning shown in (c). The red dashed line indicates the threshold intensity (≈8 mW mm⁻²) for ChR2 stimulation. As seen, despite of variations, all these 25 focuses are powerful enough for neuron stimulation, assuring the FOV of the proposed selective optogenetics. f,g) Images of the transmitted optical pattern when the skull sample is attached to the distal end of the MMF f) before and g) after wavefront shaping. h) Similar to (c), 25 focuses also can be formed after MMF plus skull. The mean of those focus is ≈237. The speckled grains are smaller than those in (a,b) as many more scattering events are involved with the addition of the skull. Photograph of a 300 μm-thick skull layer dissected from a mouse without the thinning procedure is shown in inset of (f). The scale bar is 4 μm, and it is shared by (a–c) and (f–h).

The capability of generating foci at the output of the MMF was first tested. After the TM measurement, the optimum phase mask for generating a focus at a desired location was calculated and uploaded to the DMD. The resultant optical pattern was recorded by the camera, as shown in Figure 2b. As seen, a bright focus was formed. The quality of focusing can be assessed by the ratio of the average intensity at the focal point to the average level of the background, namely, peak-to-background ratio (PBR). Moreover, by manipulating the TM and changing the phase masks on the DMD appropriately, the focal spot can be scanned across the FOV (Figure 2c) at a temporal resolution determined by the refresh rate of DMD, which is around 23 kHz and could be even faster if less DMD pixels are used; no additional MMF calibration or TM optimization is needed. The normalized intensity profile at the MMF distal end across the focal spot before and after wavefront compensation is shown in Figure 2d. The full width of half maximum (FWHM) of the focus is about $\approx 1.6\,\mu m$ and much smaller than the size of neurons (dozens of microns). The focus size could be modified by changing the distance between the focal plane and the fiber distal end.

Another important criterion for successful selective precise optogenetics is that the optical intensity of the focus should be high enough at any target location throughout the FOV, while the residual background is always sufficiently dim. To confirm that, before cell experiment, focus at 25 locations was sampled in the FOV (Figure 2c). Although the focal intensities varied spatially from 11 to 20 mW mm^{-2} (Figure 2h), all of them surpassed the threshold for effective ChR2 stimulation (8 mW mm^{-2}; indicated by the red dashed line).[54] Meanwhile, similar to the profile shown in Figure 2d, the background intensities after wavefront shaping were way below the ChR2 threshold, assuring that neurons could be stimulated only by the optical focuses.

Such capabilities of optical focusing and scanning for selective neuron stimulation can be extended to overcome the strong scattering of light due to biological tissues, such as skull and skull and brain tissue, which is imperative to achieve noninvasive deep brain optogenetics. In our system, the combination of the skull and the MMF was treated as one scattering body and the optical distortion was compensated at the same time. To demonstrate that the wavefront-shaped excitation beams can generate desired focuses through the MMF and a highly scattering skull layer, a fresh skull layer dissected from a mouse without a thinning procedure was prepared. The thickness of the dissected skull was $\approx 300\,\mu m$ (inset of Figure 2f), which was thick enough to scramble the incident focus generated by the MMF alone into a random speckled pattern. According to literature,[55] the absorption coefficient (μ_a) of a mice skull with thickness of 0.31 ± 0.05 mm is around 1.2 mm^{-1}, and the reduced scattering coefficient (μ_s') is ≈ 2.6 mm^{-1}. The dissected skull layer was then attached to the tip of MMF to mimic in vivo condition, and the scattering effects from the MMF and the skull were coupled into one TM. Speckled patterns behind the skull layer before and after wavefront shaping were recorded and shown in Figure 2f,g, respectively. As seen, a tight focus (PBR ≈ 255) could be generated at the center of the FOV after compensating the MMF and skull-induced wavefront distortions. Similar to Figure 2c, the focus was also scanned at 25 locations in the FOV after the skull, and the results are shown in Figure 2h. The mean PBR at these

25 locations is 236.9, and the standard deviation is 25.7. As extra wavefront distortions were induced by the skull, the FWHM size of the speckled grains and hence the focal spot was reduced to $\approx 0.9\,\mu m$, but the FOV could poetically be expanded compared with its peer in Figure 2a, which is consistent with earlier finding in the field.[56]

To test whether the focused light from MMF could elicit photocurrent in targeted cells, we patched a single cell (293T, of which the expression of Chr2 is confirmed in **Figure 3**a,b) under a widefield microscopy (Figure 3a). Without wavefront shaping, the output of MMF was a random speckle within the whole FOV and will not be able to achieve optically selective stimulation (Figure 3c). With wavefront shaping, one optical focus could be generated at the target region (Figure 3d, encircled by the red circle). The focus could be moved away by changing the phase masks on the DMD (Figure 3e). Note that the focuses were not generated at the absolute center of the red circle to avoid overlapping with the patch clamp, and the inward currents from the patch clamp were used to gauge the amount of ion channels that have been photostimulated. An example of the corresponding patch clamp signals is provided in Figure 3f, showing that there were inward currents when the optical focus was on the target ($t = 5$ s), which, however, reduced to almost zero when the focus was away from the target cell ($t = 10$ s). The measurement was repeated eight times, and the statistical results are given in Figure 3g, where the error bar represents the standard deviation. After that, a series of optical focuses were generated for every $\approx 9.3\,\mu m$ away from the patched cell by displaying predetermined masks on the DMD (Figure 3i). The corresponding patch clamp signals show that there are strongest currents when the optical focus is on the target (the central valley) and the inward currents decrease as the light focus is moved away from the patched cell (Figure 3j). According to the statistics of the inward currents at different optical focusing locations with respect to the central position (Figure 3k), the FWHM of the photocurrent distance function is about 15.3 μm, which is about the size of the patched cell, indicating that stimulation resolution is at single cell level.

To further confirm whether the spatially resolved photocurrent could induce selective neural activation, we performed calcium imaging on primary cortical neurons harvested from embryonic mouse brains while performing targeted photostimulation (E16). Note that the distance between the fiber facet and the target was manually enlarged for covering an appropriate FOV. To express the well-established photosensitive proteins ChR2 in neurons, we used adeno-associated virus (AAV)-based viruses with a human synapsin (hSyn) promoter, which preferentially infected neurons over other cell types. At DIV 12, the neurons were found to show EYFP fluorescence, thus confirming the neuron specificity of the ChR2 expression. For calcium imaging, a red fluorescence calcium indicator (Cal590, AAT Bioquest, USA) was used to measure the neural activation, and a background image F_b (**Figure 4**a) was obtained before any blue light illumination as the basis. The neural activity at any given time point was quantified by $\Delta F_i/F_b$, a well-established method for quantifying calcium images. The sham condition showed negligible neural activities (Figure 4b). Without wavefront shaping, light from the MMF is a random speckled pattern (inset of Figure 4c). The ratio of the difference between the
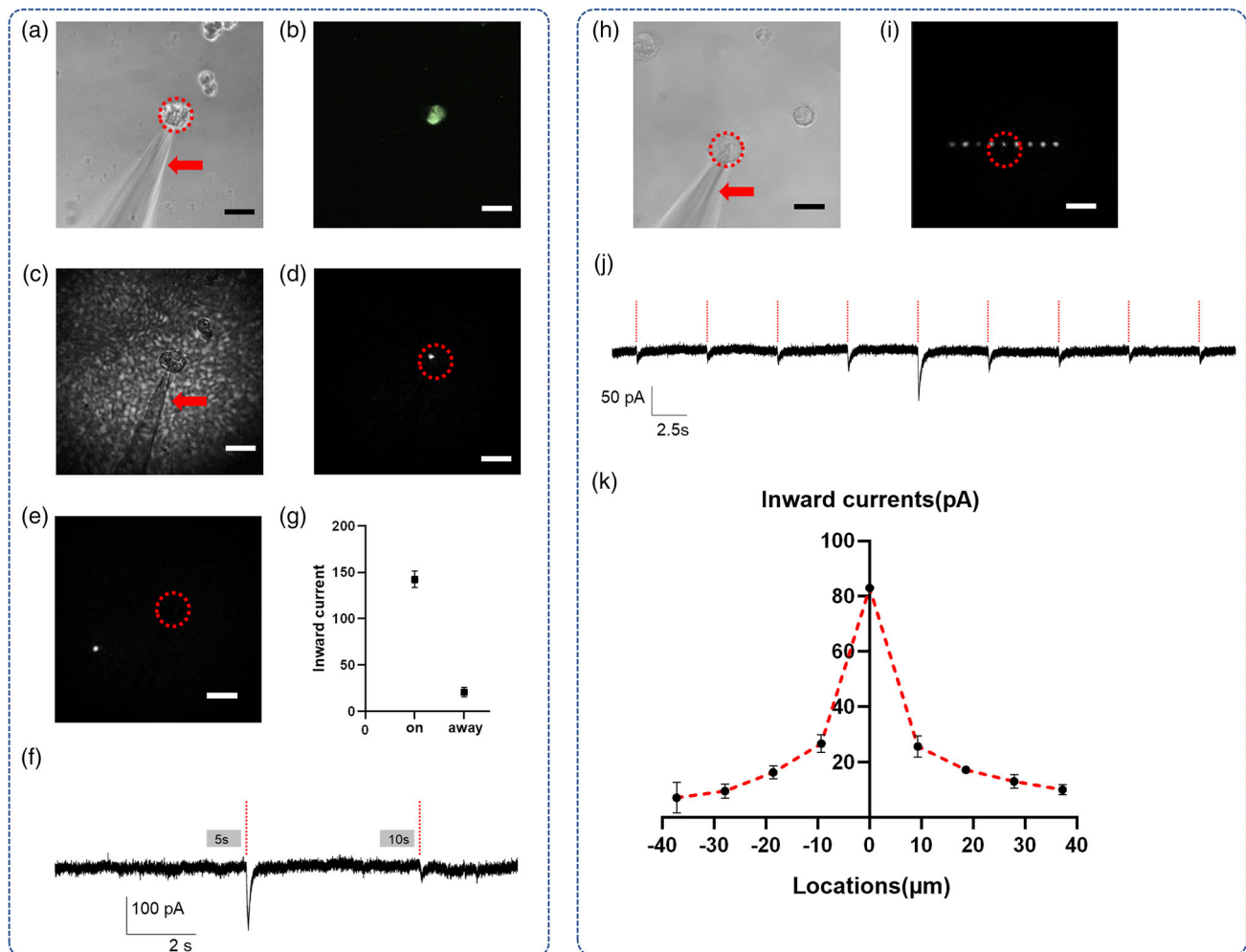
Figure 3. Evaluation of selective precise optogenetics with wavefront shaping-empowered MMF via the patch clamp system. a) The current of the target cell membrane was recorded via a patch clamp system. b) Fluorescence imaging of target cell. c) Without wavefront shaping, the output of MMF was a random speckle within the whole FOV. d,e) One optical focus was generated by wavefront shaping at the target region (encircled by the red circle) and the focus is moved away by changing the phase masks on the DMD. f) An example of the corresponding patch clamp signals, in which the red dot line is the trigger single from DMD chip. The first line ($t = 5$ s) and second line ($t = 10$ s) represent the focus of (d) and (e), respectively. g) Statistics of the inward currents recorded by the patch clamp when light focus was on and away from the target based on a measurement of eight times (the error bar is the standard deviation). h) Another cell was chosen to evaluate the resolution of optical selective stimulation. i) A series of optical focuses of the same adjacent spacing (≈ 9.3 μm) were generated one after another (not simultaneously), and the middle (circled) one overlaps with the target cell region in (h). j) The corresponding patch clamp signals, showing that there are strongest currents when the optical focus is on the target (the central valley). k) The statistics of the inward currents at different optical focusing locations with respect to the central position (the target cell and the patch clamp). The measurement was repeated five times, and the error bar is the standard deviation. Scale bar: 20 μm; the arrows in (a), (c), and (h) point to the images of the patch clamp, which touched the cell membrane directly.

recorded calcium image (F_0) and the background (F_b) with respect to the background ($\Delta F_0/F_b$) confirms that all the ChR2-eYFP positive neurons in the FOV exhibited calcium influx (Figure 4c). Then, blue light from the MMF was focused by wavefront shaping into a small region in the FOV, with a focal intensity of ≈ 15 mW mm^{-2}, as illustrated in the inset of Figure 4d. Under this condition, the corresponding ratio of differences of the calcium image and the basal calcium image F_b, denoted as ($\Delta F_1/F_b$) (Figure 4d), shows that the eYFP-ChR2 neurons in the region illuminated by focused light were activated while other neurons remained silent. Further, if the light from the

MMF was focused onto two separated regions targeting two individual neurons, as indicated in the inset of Figure 4e, the difference between the recorded calcium image and the basal calcium image ($\Delta F_2/F_b$) suggests that the two light spots induced neural activation simultaneously at the targeted neurons as expected (Figure 3e). Note that the bright spots shown in Figure 4 do not represent the focused (488 nm) light as there is filter before the detector, and the DMD only illuminated the neurons by 30 ms, which is much shorter than the duration of fluorescence signal at the bright spot. Therefore, the possibility of bright signals (which has longer time duration) caused by the leakage of
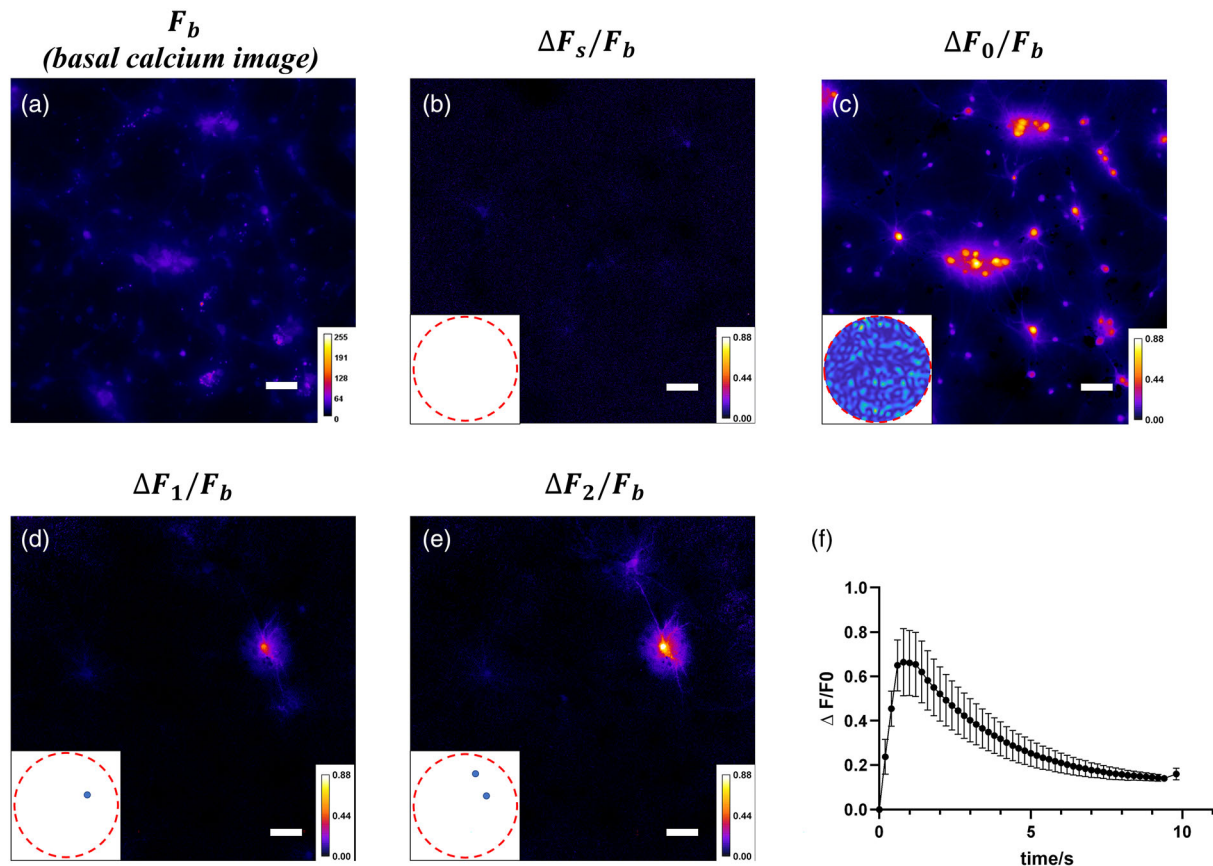
**ADVANCED
SCIENCE NEWS**

www.advancedsciencenews.com

**ADVANCED
PHOTONICS
RESEARCH**
Open Access

www.adpr-journal.com

Figure 4. In vitro demonstration of selective precise optogenetics with wavefront shaping-empowered MMF. Calcium images were acquired by an epifluorescence imaging system. a) Calcium imaging before the blue light illumination, serving as the background (F_b). b) The cultured neurons were quiet without photostimulation in sham condition. c) Without wavefront shaping, light from the MMF is a random speckled pattern. The difference ($\Delta F_0/F_b$) between the recorded calcium image and the background confirms that all the ChR2-eYFP positive neurons in the FOV exhibited calcium influx. d,e) Based on the obtained TM, the phase masks for generating one and two focal regions (as illustrated in the insets) can be calculated and uploaded to the DMD. The corresponding differences of the calcium images with respect to background images are shown in (d) and (e), respectively, confirming selective activation of ChR2 selectively for precise neural activation with controlled light pattern from the MMF. f) The statistics of repeated stimulation of the target cell in (d). The scale bars in (a−e) are 50 μm.

focused light spots should be ignored. In Figure 4f, the dynamics of $\Delta F/F_b$ in response to focus light stimulation from MMF is shown as a function of time over repeated stimulations (five times). It can be seen that the neuron activity lasts for a few seconds, and there is a delay of ≈1 s between the onset of neuron response with light stimulation that is applied at $t = 0$ s. These groups of experiments validate the proposed idea that focused light from the MMF can activate ChR2 selectively for precise neural activation.

3. Discussion

In this work, a new strategy of using economic and common MMF combined with wavefront shaping to perform optically selective neuron stimulation is proposed and experimentally demonstrated. The attractiveness of such an approach is that the single-cell-level optical focusing can be spatially manipulated and hence the active selection for neuron stimulation can be electronically realized instead of embedding mechanical actuators

with MMF. Moreover, the high-resolution focusing and stimulation capabilities can penetrate through highly scattering media, such as the MMF itself and a mouse skull, as shown in Figure 2. These are not possible with a regular fiber or other optical delivery techniques currently used in optogenetics.

It is very interesting to examine the optical fields at the exit of the MMF alone and the MMF plus skull. First, the measured FWHM values of focal spots were reduced from ≈1.6 to ≈0.9 μm under the same condition, which is due to the increase in scattering events in the skull that further scrambles light propagation. This phenomenon is consistent with literature finding that adding a highly scattering medium to an imaging system can equivalently increase the numerical aperture (NA),[56,57] creating tighter diffraction-limited light spots. It may potentially open up new venues to achieve high-resolution or even super-resolution neuron stimulation and imaging simultaneously with wavefront shaping-assisted MMF. Second, the scattering of the skull also breaks the FOV limitation of MMF. At the same working distance, MMF with the skull could potentially result in a

larger FOV. This allows selective neuron stimulation and imaging (although not demonstrated herein as it is beyond the scope of the current work) in a larger FOV. Third, it is noticed that the depth focus along the optical axis is also considerably reduced when light transmits through the skull. As measured, the depth of wavefront shaping-enabled focuses for MMF and MMF plus skull are ≈35 and ≈10 µm (FWHM), respectively. Such contrast is also consistent with the increased effective NA with the additional skull. It potentially provides excellent optical sectioning capability along the optical axis, allowing for 3D selective neuron stimulation and imaging, which is beyond the scope of current manuscript but will be explored in the next phase.

Notably, wavefront shaping-empowered optical focusing was achieved in a transmission mode. Theoretically it can be applied for in vivo experiments, but after precalibration, the stability of the MMF shall be kept well during the whole process of TM calibration, fiber injection, and neuron experiments to avoid significant deformation to the fiber. Otherwise, the TM will be changed and the calibration procedure needs to be conducted again. A design of MMF for less sensitivity to deformations may be one of the solutions, but it will increase the cost and limit the applications. For example, some special MMFs have a perfectly parabolic refractive index profile and are insensitive to deformations like bending.[58] These fibers, however, are currently not commercially available and beyond our accessibility. Modifying the present setup into refection geometry to achieve real-time calibration and reoptimization at the proximal end of the MMF may be another solution; in this scenario, selective optogenetics can also be conducted even when the fiber is deformed or the experiment sample is under motion. Although it may complicate the optical setup and computation of the TM of the MMF,[59] the need for special MMF can be avoided. With the development of wavefront modulators and optimization algorithms, the speed and adaptivity of the calibration can also be improved. For example, real-time resilient focusing through MMF has been reported,[60] and a dynamic mutation algorithm has been proposed to automatically adapt moderate perturbations to the MMF and maintain or even recover the optical focusing performance.[45]

Three more aspects have to be clarified before conclusion. First, to accomplish noninvasive MMF-based optical focusing and neuron stimulation at depths, feedback signals that are closely related to the in situ optical intensity are required for MMF TM measurement. In this regard, photoacoustic[26,28,61] or fluorescent[62–64] signals may provide promising virtual or physical internal guidestars, assuming that the resultant focal spot is sufficient tight for selective optogenetics. Second, the current setup uses one-photon excitation for photoactivation in optogenetics. Therefore, the application was limited to a brain region where labeled cells were relatively sparsely distributed. To reduce contribution coming from the out-of-focus dendritic or axonal processes and thus, to improve the resolution of photostimulation along the optical axis, some approaches, such as only expressing the opsins in the soma and/or axion hillock, will be considered in future work. Last but not the least, it will be aimed to achieve fluorescence imaging,[65–67] and selective optogenetics with a single MMF and then to monitor brain activities while controlling the targeted neurons in the next step. Nonetheless, the present work provides the first demonstration

of utilizing wavefront shaping-empowered MMF toward deep-brain, noninvasive, or minimally optogenetic studies, which offers large degrees of freedom in controlling light propagation and stimulation in previously inaccessible brain regions.

4. Conclusion

In summary, this study proposes an innovative approach for deep-tissue selective precise neuron stimulation via the integration of wavefront shaping and MMF. The concept was preliminarily demonstrated by showing that primary neurons expressing Chr2 can be regulated spatiotemporally in the experiment. The unique capability of achieving focused light delivery and fast raster scanning of the optical focus at the distal end of the MMF and through a dissected skull opens new venues for deep-penetrating noninvasive optically selective optogenetics. For tissue regions beyond the limit of wavefront shaping or lacking reliable guidestars, our system is still feasible as the MMF can be implanted near the targeted tissue region to reduce the scattering effect to light. Compared with other existing approaches, the small size of the MMF can minimize the insertion damages to brain tissues, offering a minimally invasive operation.

5. Experimental Section

Optical setup: The proposed system is illustrated in **Figure 5**. An externally trigged laser operating at 488 nm (OBIS, Coherent, USA) was used as the light source for neuron stimulation. Its output (up to 150 mW) was expanded by L_1 and L_2 and then reflected and modulated by a DMD (1,024 × 768 pixels, V-7001, Vialux, Germany) before being relayed (via L_3 and L_4) and coupled (via L_5) into a 1 m-long MMF (0.22 NA, core diameter 50 µm, FG050LGA, Thorlabs, USA) which contained more than 2,500 modes. The output optical field at the distal end of the MMF was recorded by a complementary metal oxide semiconductor camera (BFS-U3-04S2C-CS, FLIR, USA), which was synchronized with the DMD and the optimal pattern calculation. In experiment, the framerate of the DMD was set at ≈500 Hz to adapt the speed of the camera for calibration. After that, DMD worked at 22 kHz for raster scanning of the focus. Imaging of neuron cells was obtained by an epifluorescence microscopy system (IX73, Olympus, USA) to monitor the optogenetics results. Note that due to the flexibility of the MMF, the optical excitation module and the sample were not necessarily closely positioned in application, opening potentials for wearable apparatus (e.g., only the fiber distal end mounted on the mouse head) with remote control.

Algorithm Implementation: As a binary diffraction device, DMD was often used for high-resolution amplitude modulation. In this study, DMD was performed as a phase modulator for higher modulation efficiency (≈5 times), meanwhile, with a refresh rate (up to 23 kHz) much faster than that of liquid crystal-based spatial light modulator. The phase modulation was realized by the Lee hologram method proposed by Conkey et al.[68] In this method, the desired phase distribution was encoded in a binary computer-generated hologram (CGH) that was displayed on the DMD, where $n \times n$ superpixels were homogeneously distributed on the screen. In this study, the DMD had 1024 × 768 independent pixels (24 × 16 pixels were combined to form one superpixel) and the DMD modulation region was composed of 32 × 32 superpixels at the center, surrounded by a reference region that was all set to be 1.

To achieve a phase modulation of the target phase mask with DMD, a new amplitude hologram was digitally generated by the interference of the target (x, y are space coordinates) phase mask $\tilde{U} = \exp(j\varphi(x,y))$ and the off-axis reference beam $\tilde{R} = \exp(j2\pi\alpha(x - y))$.
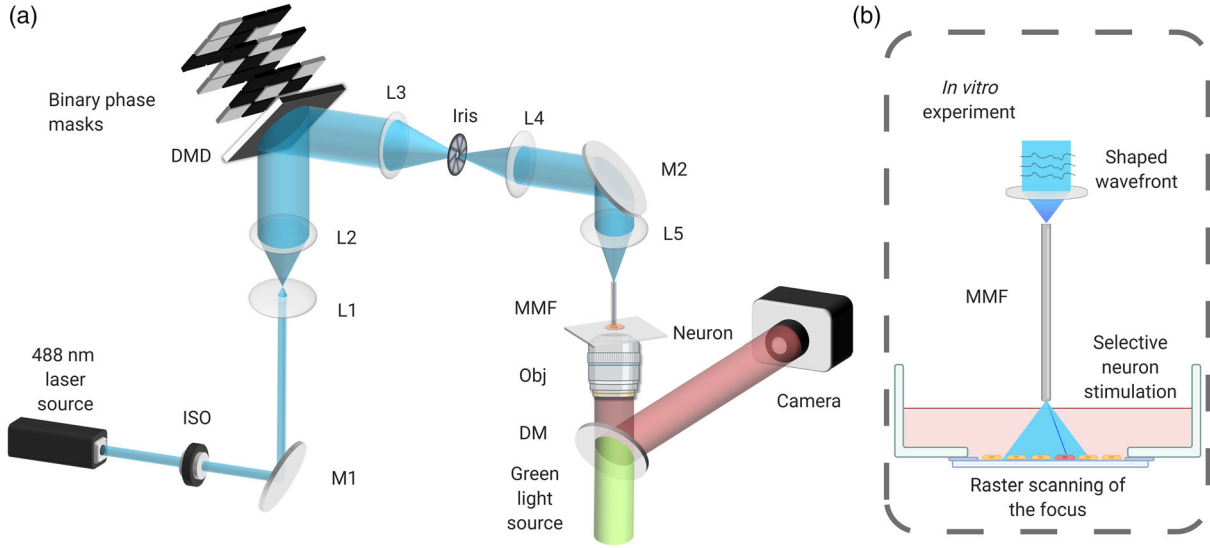
Figure 5. Illustration of the proposed system. a) Schematic of the optical setup. M$_{1-2}$: mirrors; L$_{1-5}$: lenses; DMD: digital micromirror device; Obj: objective; DM: Dichroic Mirrors. A same camera is used for MMF calibration and epifluorescence imaging in cell experiments. After calibration, cultured samples are placed at the focal plane of the MMF output field. The capacity of the system is tested with a skull attached to the distal end of the MMF. b) After calibration, raster scanning of the focus and hence selective optogenetics could be achieved by displaying predetermined phase masks consecutively on the DMD screen.

$$t(x,y) = |\tilde{U} + \tilde{R}|^2 = \frac{1}{2} + \frac{1}{4}e^{j2\pi(x-y)\alpha}e^{-j\varphi(x,y)} + \frac{1}{4}e^{-j2\pi(x-y)\alpha}e^{j\varphi(x,y)} \quad (1)$$

If the carrier frequency α was higher than the maximal spatial frequency of $\varphi(x,y)$, three distinct orders (+1, 0, −1) of diffraction were obtained, with large separation among different orders, as shown in **Figure 6**. In experiment, a 4-f system was used, and an iris was positioned at the Fourier plane for spatial filtering to select the −1 order beam, which encoded the desired phase distribution of the target phase mask $\tilde{U}$.

As the pixels on the DMD, as shown in Figure 6, can only be set to 0 or 1, a binary amplitude hologram was generated by thresholding the previous amplitude hologram (Equation (1)) as follows.

$$t(x,y) = 0.5 + 0.5\cos(2\pi(x-y)\alpha - \varphi(x,y)); h(x,y) = \begin{cases} 1; t(x,y) > 0.5 \\ 0; otherwise \end{cases} \quad (2)$$

Consequently, the bright fringe and its spatial coordinate met the following relation

$$2\pi(x-y)\alpha - \varphi(x,y) = 2n\pi \mp \frac{\pi}{2} (n = 1, 2 \ldots) \quad (3)$$

As the TM of the system relates the input optical field (E_{in}) to the output field (E_{out}), described as $E_{out} = T \times E_{in}$, we calculated the TM once the complex output and input fields were obtained, that is, $T = E_{out} \times (E_{in})^{-1}$. In this study, for the input basis, we chose Hadamard matrix (H) as it perfectly fit the requirements: first, the experimental signal-to-noise ratio (SNR) was improved as the elements of this matrix were either +1 or −1; second, using the inverse property of Hadamard matrix, the calculation of TM can be simplified to

$$T = E_{out} \times H^T \quad (4)$$

Because the camera can only capture the intensity of output field, here, we adopted a phase-shifting algorithm to record the complex optical field.[69] If the modulation part was shifted by a phase of ω, the m_{th} output intensity mode could be expressed by

$$I_m^\omega = |s_m + \sum_n e^{i\omega}T_{mn}E_n^{in}|^2$$
$$= |s_m|^2 + |\sum_n e^{i\omega}T_{mn}E_n^{in}|^2 + 2\text{Re}\{\bar{s}_m e^{i\omega}\sum_n T_{mn}E_n^{in}\} \quad (5)$$

Here, s_m denotes the complex field in the m_{th} output mode induced by the reference part, E_n^{in} is the n_{th} input mode, and T_{mn} is the (m, n) element of the TM. With the four-phase shifts of the Hadamard basis $(0, \pi/2, \pi, 3\pi/2)$, the output mode E_m^{out} was coupled with s_m (the static reference mask) as

$$\frac{(I_m^0 - I_m^\pi)}{4} + i\frac{(I_m^{3\pi/2} - I_m^{\pi/2})}{4} = s_m\sum_n T_{mn}E_n^{in} = s_m E_m^{out} \quad (6)$$

Thus, the observed complex TM could be given by

$$T_{obs} = E_{obsout} \times E_{in}^{-1} = S_{ref} \times T \quad (7)$$

where s_{ref} is a diagonal matrix representing the static reference input. As s_{ref} is stationary over time, T_{obs} is directly proportional to T.

As the TM measurement involved N segments on the DMD, the number of patterns projected on the DMD screen was $4N$ in experiment. These patterns were the same for the calibration process in different scenarios, so that they could be preloaded to the onboard memory and then electronically refreshed at very fast speed in the experiment. For focusing at each position, the corresponding row of the TM was used to provide conjugation and generate the CGH before uploading to the DMD. After the TM measurement, the focal spot can be scanned throughout the FOV, as shown in Figure 2c.

293T Harvest: Human embryonic kidney (HEK) 293T cells were purchased from ATCC. It was maintained in Dulbecco's Modified Eagle Medium (DMEM), supplemented with 10% FBS, 10% Penicillin−Streptomycin (all from Gibco), inside a humidified incubator 37 °C with 5% CO$_2$. For patch clamp recording, cells were seeded in 35 mm culture dishes at 1×10^5 cells per dish, allowed to grow overnight, and transfected with ChR2 on next day.

**ADVANCED
SCIENCE NEWS**
www.advancedsciencenews.com

**ADVANCED
PHOTONICS
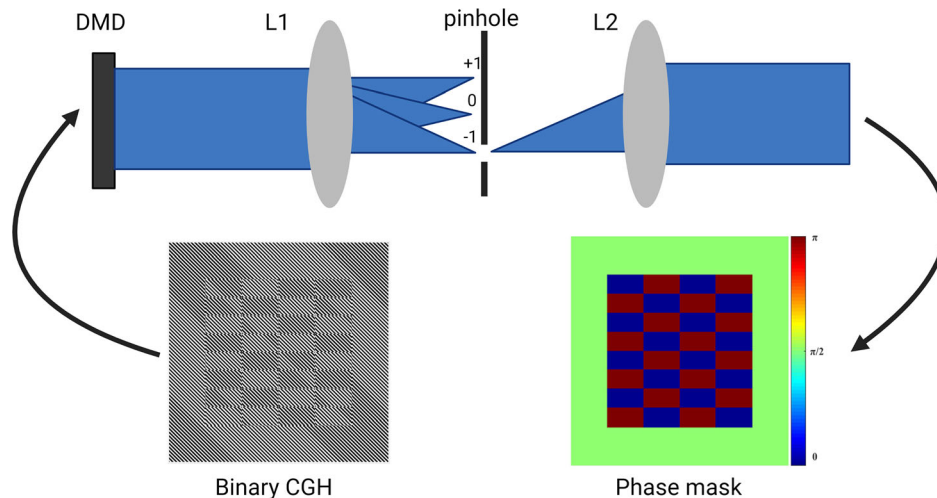RESEARCH**
Open Access
www.adpr-journal.com

Figure 6. Illustration of the DMD-based phase modulation. The binary Lee hologram encodes the phase mask displayed on the DMD, from which light is diffracted. Only the −1-order beam transmits through the small pinhole and is encoded with the target phase mask. L1 and L2 are a pair of lenses that construct a 4-f system.

Plasmid Transfection: The plasmid pcDNA3.1-ChR2-IRES-GFP was purchased from Dr. Ardem Patapoutian. Cells were transfected using the Lipofectamine 2000 kit (Invitrogen). 3.0 μg plasmid and 5 μL of Lipofectamine 2000 were complexated in Opti-MEM medium (Gibco) according to the manufacturer's instructions and added to the cells. The cells were used for further experiments 24 h later.

293T Cell Patch Clamp Recording: After completing Chr2 transfection, cells were directly used for patch clamp recording. Borosilicate glass-made patch pipettes (Vitrex, Modulohm A/S, Herlev, Denmark) were pulled with a micropipette puller (P-97, Sutter Instrument Co., USA) to a resistance of 2−5 MO before being filled with KCl pipette solution (in mM): KCl 138, NaCl 10, MgCl$_2$ 1, and HEPES 10 with D-manitol compensated for osm 290. Inward current was recorded with a data acquisition system (DigiData 1322 A, Axon Instruments) and an amplifier (Axopatch-200B, Axon Instruments, Foster City, CA, USA). The command voltages were controlled by a computer equipped with pClamp Version 9 software. When the whole-cell Giga seal was formed and the capacitance of cell was measured, inward currents were measured by a voltage clamp gap free recording and then moved the fiber to the target cells for light stimulation. Cells placed on bath solution (in mM): NaCl 130, MgCl$_2$ 2, KCl 4.5, glucose 10, HEPES 20, and CaCl$_2$ 2, pH 7.4 during the whole process.

Primary Cortical Neuron Harvest: Primary cultures of the cortices of mouse embryos at embryonic day 16 were obtained as reported.[70] Briefly, cortices were dissected in ice-cold Neurobasal medium (Gibco Invitrogen Corporation. Carlsbad, CA) and incubated in 0.25% trypsin-EDTA (Gibco Invitrogen Corporation. Carlsbad, CA) for 15 min. The cells were centrifuged and washed in Neurobasal medium containing 10% FBS, 0.25% L-glutamine, and 1% penicillin−streptomycin (all from Gibco Invitrogen Corporation. Carlsbad, CA) and then centrifuged again. Afterward, the cells were resuspended in the medium and gently mechanically triturated with a pipette and then allowed to stand for 15 min. The resultant supernatant was discarded, and the cells were resuspended in the abovementioned medium further, supplemented with 2% B27 serum-free supplement (Gibco Invitrogen Corporation. Carlsbad, CA). The cells were plated at 5×10^5 cells in 35 mm dishes containing coverslips coated with poly-L-lysine (PLL) or at 1×10^5 cells into PLL-coated confocal dishes. After 24 h, the medium was changed to Neurobasal + 2% B27 + 0.25% L-glutamine + 1% penicillin−streptomycin. The medium was half changed every 72 h.

Viral Transduction: Viruses were packaged by BrainVTA Co. Ltd. (Wuhan, China), and all viral aliquots were placed at −80 °C prior to use. We used a rAAV-9 vector, with a human synapsin (hSyn) promoter, which enabled the viruses to preferentially transduct neurons. The ChR2 sequence was fused with either fluorescent reporter EYFP or Ca2 + sensor protein GCaMP6S and a polyA tag at the end of the sequence. The viruses used in this study were rAAV/9-hSyn-EYSP-pA and rAAV/9-hSyn-ChR2-EYFP-pA.

Primary neurons were transduced with at DIV 7 using viruses diluted 1/10 in PBS at room temperature. For every 5×10^5 primary neurons seeded, 109 genome copies (GC) of the CTRL virus and 1010 GC of the ChR2 virus were added directly into the cell medium. The plates were gently shaken and placed in the incubator. Cells were allowed to incubate for 4–5 days while being monitored for fluorescence and cell conditions, after which they were used for further experiments.

Mouse Skull Preparation: Male C57BL/6J mice, at the age of 8–12 weeks, were obtained from the Central Animal Facility (CAF) of The Hong Kong Polytechnic University. Mice were raised under standard conditions with fresh water and food available ad libitum. All experiments were performed according to the animal (control of experiments) regulations and were approved by Department of Health of Hong Kong SAR. A mouse head was obtained by decapitation. The scalp was then removed with spring scissors, and lateral muscles were retracted to expose as much skull surface as possible. The back of the skull was opened by making a cut caudal to the cerebellum, and the skull was cut along squamosal so that the parietal and frontal was obtained as complete as possible. Tissues attached to the skull were carefully removed with fine scissors; after that, the skull was rinsed with water and ethanol several times.

Experiment Procedure: In this study, wavefront shaping was implemented to achieve optical focusing and raster scanning of the focal point at the distal end of the MMF, based on which, single neurons within the FOV were selectively excited. The in vitro system shown in Figure 5 was developed and configured to test the feasibility of the concept, with a DMD for fast wavefront modulation and temporal controlling of the focal spot. Even though the tau off kinetics of current opsins range above 1 ms, with high temporal modulation, our system can perform precise optogenetics according to the specific spatiotemporal sequence. In addition to the wavefront modulating module for excitation beam, the system also consisted of a fluorescence imaging module for measuring the cellular responses. In the experiment, the optical propagation path, from the DMD screen to the desired focal plane after the distal end of the MMF, was expressed as a TM. The detailed process of measuring the TM was described earlier. The phase masks to be uploaded on the DMD screen for focusing light at the desired locations on the MMF focal plane were calculated based on the TM. If the optical focus and one of the

cultured neurons (assuming they are sparsely distributed in the sample) spatially overlap, that specific neuron is activated while all other neurons remain silent. By changing the phase mask display on the DMD, high spatiotemporal optical focusing at the focal plane, and hence the selective optogenetics, were achieved. To monitor the fluorescence emission associated with neuron activities, the cultured neurons were placed in a commercially epifluorescence imaging system at the focal plane of the MMF. A standard commercially available MMF with a core of $50\,\mu m$ in inner diameter and a NA of 0.22 was used in experiment. Once the fiber was placed and aligned with the epifluorescence imaging system, it took ≈ 2 mins to obtain the TM, compute a FOV of $60 \times 60\,\mu m^2$ at the focal plane, and upload the desired phase patterns to the on-board memory of the DMD.

Conflict of Interest

The authors declare no conflict of interest.

Author Contributions

T.Z. and Z.Q. contributed equally to this work. T.Z., Z.Q., L.S., and P.L. conceived the idea. T.Z. and Z.Q. conducted the experiment and processed the data. T.Z. and Y.W. conducted the patch clamp experiments. Z.Y. and H.L. helped build the optical setup. T.Z., Z.Q., and P.L. wrote the manuscript. J.T., L.S., and P.L. supervised the project. All members contributed to the discussion of the results and proofreading of the manuscript.

Data Availability Statement

The data that support the findings of this study are available from the corresponding author upon reasonable request.

[1] H. T. Greely, C. Grady, K. M. Ramos, W. Chiong, J. Eberwine, N. A. Farahany, L. S. M. Johnson, B. T. Hyman, S. E. Hyman, K. S. Rommelfanger, *J. Neurosci.* **2018**, *38*, 10586.

[2] *Nat. Methods* **2018**, *15*, 839.

[3] L. Fan, *Innovation* **2021**, *2*, 100073.

[4] W. Koroshetz, J. Gordon, A. Adams, A. Beckel-Mitchener, J. Churchill, G. Farber, M. Freund, J. Gnadt, N. S. Hsu, N. Langhals, *J. Neurosci.* **2018**, *38*, 6427.

[5] A. P. Alivisatos, M. Chun, G. M. Church, R. J. Greenspan, M. L. Roukes, R. Yuste, *Neuron* **2012**, *74*, 970.

[6] F. Zhang, A. M. Aravanis, A. Adamantidis, L. de Lecea, K. Deisseroth, *Nat. Rev. Neurosci.* **2007**, *8*, 577.

[7] S. Luan, I. Williams, K. Nikolic, T. G. Constandinou, *Front. Neuroeng.* **2014**, *7*, 27.

[8] M. C. Mott, J. A. Gordon, W. J. Koroshetz, *PLoS Biol.* **2018**, *16*, 3000066.

[9] F. Pisano, M. Pisanello, S. J. Lee, J. Lee, E. Maglie, A. Balena, L. Sileo, B. Spagnolo, M. Bianco, M. Hyun, *Nat. Methods* **2019**, *16*, 1185.

[10] F. Zhang, M. Prigge, F. Beyrière, S. P. Tsunoda, J. Mattis, O. Yizhar, P. Hegemann, K. Deisseroth, *Nat. Neurosci.* **2008**, *11*, 631.

[11] S. Chen, A. Z. Weitemier, X. Zeng, L. He, X. Wang, Y. Tao, A. J. Huang, Y. Hashimotodani, M. Kano, H. Iwasaki, *Science* **2018**, *359*, 679.

[12] N. C. Klapoetke, Y. Murata, S. S. Kim, S. R. Pulver, A. Birdsey-Benson, Y. K. Cho, T. K. Morimoto, A. S. Chuong, E. J. Carpenter, Z. Tian, *Nat. Methods* **2014**, *11*, 338.

[13] K. Erbguth, M. Prigge, F. Schneider, P. Hegemann, A. Gottschalk, *PloS One.* **2012**, *7*, 46827.

[14] I.-W. Chen, E. Ronzitti, B. R. Lee, T. L. Daigle, D. Dalkara, H. Zeng, V. Emiliani, E. Papagiakoumou, *J. Neurosci.* **2019**, *39*, 3484.

[15] D. Oron, E. Papagiakoumou, F. Anselmi, V. Emiliani, *Prog. Brain Res.* **2012**, *196*, 119.

[16] O. A. Shemesh, D. Tanese, V. Zampini, C. Linghu, K. Piatkevich, E. Ronzitti, E. Papagiakoumou, E. S. Boyden, V. Emiliani, *Nat. Neurosci.* **2017**, *20*, 1796.

[17] N. Ji, *Neuron* **2014**, *83*, 1242.

[18] P. Andersen, R. Morris, D. Amaral, T. Bliss, J. O'Keefe, *The Hippocampus Book*, Oxford University Press, Oxford **2006**.

[19] T. Misgeld, M. Kerschensteiner, *Nat. Rev. Neurosci.* **2006**, *7*, 449.

[20] I. M. Vellekoop, A. Mosk, *Opt. Lett.* **2007**, *32*, 2309.

[21] A. P. Mosk, A. Lagendijk, G. Lerosey, M. Fink, *Nat. Photonics* **2012**, *6*, 283.

[22] M. Nixon, O. Katz, E. Small, Y. Bromberg, A. A. Friesem, Y. Silberberg, N. Davidson, *Nat. Photonics* **2013**, *7*, 919.

[23] J. Bertolotti, E. G. van Putten, C. Blum, A. Lagendijk, W. L. Vos, A. P. Mosk, *Nature* **2012**, *491*, 232.

[24] I. M. Vellekoop, A. Lagendijk, A. Mosk, *Nat. Photonics* **2010**, *4*, 320.

[25] R. Horstmeyer, H. Ruan, C. Yang, *Nat. Photonics* **2015**, *9*, 563.

[26] P. Lai, L. Wang, J. W. Tay, L. V. Wang, *Nat. Photonics* **2015**, *9*, 126.

[27] O. Tzang, E. Niv, S. Singh, S. Labouesse, G. Myatt, R. Piestun, *Nat. Photonics* **2019**, *13*, 788.

[28] T. Chaigne, O. Katz, A. C. Boccara, M. Fink, E. Bossy, S. Gigan, *Nat. Photonics* **2014**, *8*, 58.

[29] T. Čižmár, M. Mazilu, K. Dholakia, *Nat. Photonics* **2010**, *4*, 388.

[30] A. Boniface, M. Mounaix, B. Blochet, R. Piestun, S. Gigan, *Optica* **2017**, *4*, 54.

[31] S. Yoon, M. Kim, M. Jang, Y. Choi, W. Choi, S. Kang, W. Choi, *Nat. Rev. Phys.* **2020**, *2*, 141.

[32] O. Katz, P. Heidmann, M. Fink, S. Gigan, *Nat. Photonics* **2014**, *8*, 784.

[33] S. Rotter, S. Gigan, *Rev. Mod. Phys.* **2017**, *89*, 015005.

[34] S. Popoff, G. Lerosey, M. Fink, A. C. Boccara, S. Gigan, *New J. Phys.* **2011**, *13*, 123021.

[35] J. Yoon, M. Lee, K. Lee, N. Kim, J. M. Kim, J. Park, H. Yu, C. Choi, W. Do Heo, Y. Park, *Sci. Rep.* **2015**, *5*, 13289.

[36] H. Ruan, J. Brake, J. E. Robinson, Y. Liu, M. Jang, C. Xiao, C. Zhou, V. Gradinaru, C. Yang, *Sci. Adv.* **2017**, *3*, eaao5520.

[37] R. P. Barretto, T. H. Ko, J. C. Jung, T. J. Wang, G. Capps, A. C. Waters, Y. Ziv, A. Attardo, L. Recht, M. J. Schnitzer, *Nat. Med.* **2011**, *17*, 223.

[38] S. L. Resendez, J. H. Jennings, R. L. Ung, V. M. K. Namboodiri, Z. C. Zhou, J. M. Otis, H. Nomura, J. A. McHenry, O. Kosyk, G. D. Stuber, *Nat. Protoc.* **2016**, *11*, 566.

[39] N. Accanto, I. W. Chen, E. Ronzitti, C. Molinier, C. Tourain, E. Papagiakoumou, V. Emiliani, *Sci. Rep.* **2019**, *9*, 7603.

[40] V. Szabo, C. Ventalon, V. De Sars, J. Bradley, V. Emiliani, *Neuron* **2014**, *84*, 1157.

[41] M. E. Bocarsly, W.-C. Jiang, C. Wang, J. T. Dudman, N. Ji, Y. Aponte, *Biomed. Opt. Express* **2015**, *6*, 4546.

[42] H.-T. Xu, F. Pan, G. Yang, W.-B. Gan, *Nat. Neurosci.* **2007**, *10*, 549.

[43] P. Moshayedi, G. Ng, J. C. Kwok, G. S. Yeo, C. E. Bryant, J. W. Fawcett, K. Franze, J. Guck, *Biomaterials* **2014**, *35*, 3919.

[44] T. Čižmár, K. Dholakia, *Opt. Express* **2011**, *19*, 18871.

[45] H. Li, C. M. Woo, T. Zhong, Z. Yu, Y. Luo, Y. Zheng, X. Yang, H. Hui, P. Lai, *Photonics Res.* **2021**, *9*, 202.

[46] Z. Wu, J. Luo, Y. Feng, X. Guo, Y. Shen, Z. Li, *Opt. Express* **2019**, *27*, 5570.

[47] Y. Choi, C. Yoon, M. Kim, T. D. Yang, C. Fang-Yen, R. R. Dasari, K. J. Lee, W. Choi, *Phys. Rev. Lett.* **2012**, *109*, 203901.

[48] I. N. Papadopoulos, S. Farahi, C. Moser, D. Psaltis, *Opt. Express* **2012**, *20*, 10583.

[49] O. Tzang, A. M. Caravaca-Aguirre, K. Wagner, R. Piestun, *Nat. Photonics* **2018**, *12*, 368.

[50] T. Zhong, Z. Yu, H. Li, Z. Li, H. Li, P. Lai, *J. Innovation Opt. Health Sci.* **2019**, *12*, 1942007.

[51] I. T. Leite, S. Turtaev, X. Jiang, M. Šiler, A. Cuschieri, P. S. J. Russell, T. Čižmár, *Nat. Photonics* **2017**, *12*, 33.

[52] M. Plöschner, T. Tyc, T. Čižmár, *Nat. Photonics* **2015**, *9*, 529.

[53] M. Plöschner, V. Kollárová, Z. Dostál, J. Nylk, T. Barton-Owen, D. E. Ferrier, R. Chmelík, K. Dholakia, T. Čižmár, *Sci. Rep.* **2015**, *5*, 18050.

[54] E. S. Boyden, F. Zhang, E. Bamberg, G. Nagel, K. Deisseroth, *Nat. Neurosci.* **2005**, *8*, 1263.

[55] H. Soleimanzad, H. Gurden, F. Pain, *J. Biomed. Opt.* **2017**, *22*, 010503.

[56] I. N. Papadopoulos, S. Farahi, C. Moser, D. Psaltis, *Opt. Lett.* **2013**, *38*, 2776.

[57] Y. Choi, T. D. Yang, C. Fang-Yen, P. Kang, K. J. Lee, R. R. Dasari, M. S. Feld, W. Choi, *Phys. Rev. Lett.* **2011**, *107*, 023902.

[58] D. E. B. Flaes, J. Stopka, S. Turtaev, J. F. De Boer, T. Tyc, T. Čižmár, *Phys. Rev. Lett.* **2018**, *120*, 233901.

[59] R. Y. Gu, R. N. Mahalati, J. M. Kahn, *Opt. Express* **2015**, *23*, 26905.

[60] A. M. Caravaca-Aguirre, E. Niv, D. B. Conkey, R. Piestun, *Opt. Express* **2013**, *21*, 12881.

[61] D. B. Conkey, A. M. Caravaca-Aguirre, J. D. Dove, H. Ju, T. W. Murray, R. Piestun, *Nat. Commun.* **2015**, *6*, 1.

[62] I. M. Vellekoop, E. Van Putten, A. Lagendijk, A. Mosk, *Opt. Express* **2008**, *16*, 67.

[63] J. Tang, R. N. Germain, M. Cui, *Proc. Natl. Acad. Sci.* **2012**, *109*, 8434.

[64] A. Boniface, J. Dong, S. Gigan, *Nat. Commun.* **2020**, *11*, 1.

[65] S. Turtaev, I. T. Leite, T. Altwegg-Boussac, J. M. P. Pakan, N. L. Rochefort, T. Cizmar, *Light: Sci. Appl.* **2018**, *7*, 92.

[66] S. A. Vasquez-Lopez, R. Turcotte, V. Koren, M. Ploschner, Z. Padamsey, M. J. Booth, T. Cizmar, N. J. Emptage, *Light: Sci. Appl.* **2018**, *7*, 110.

[67] S. Ohayon, A. Caravaca-Aguirre, R. Piestun, J. J. DiCarlo, *Biomed. Opt. Express* **2018**, *9*, 1492.

[68] D. B. Conkey, A. M. Caravaca-Aguirre, R. Piestun, *Opt. Express* **2012**, *20*, 1733.

[69] S. M. Popoff, G. Lerosey, R. Carminati, M. Fink, A. C. Boccara, S. Gigan, *Phys. Rev. Lett.* **2010**, *104*, 100601.

[70] Z. Qiu, J. Guo, S. Kala, J. Zhu, Q. Xian, W. Qiu, G. Li, T. Zhu, L. Meng, R. Zhang, *iScience* **2019**, *21*, 448.